


Ultrathin ZnS Single Crystal Nanowires: Controlled Synthesis and Room-Temperature Ferromagnetism Properties

Guoxing Zhu,^{†,§} Shuguang Zhang,^{‡,||} Zheng Xu,^{*,†} Jing Ma,[‡] and Xiaoping Shen[§]

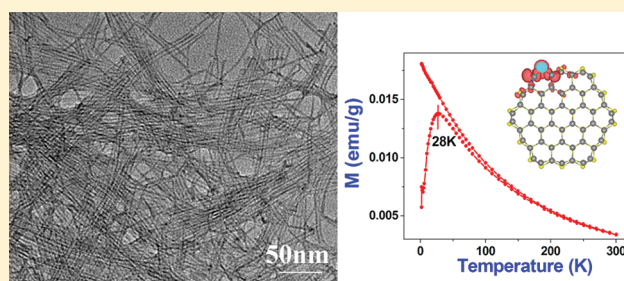
[†]State Key Laboratory of Coordination Chemistry, School of Chemistry and Chemical Engineering, Nanjing National Laboratory of Solid State Microstructure, and [‡]School of Chemistry and Chemical Engineering, Institute of Theoretical and Computational Chemistry, Key Laboratory of Mesoscopic Chemistry of MOE, Nanjing University, Nanjing 210093, China

[§]School of Chemistry and Chemical Engineering, Jiangsu University, Zhenjiang 212013, China

^{||}School of Chemical Engineering, Shandong University of Technology, Zibo 255049, China

 Supporting Information

ABSTRACT: Highly uniform single crystal ultrathin ZnS nanowires (NWs) with 2 nm diameter and up to 10 μm length were fabricated using a catalyst-free colloidal chemistry strategy. The nanowires crystallized in hexagonal phase structure with preferential growth along the direction of the (001) basal plane. The strong polarity of the (001) plane composed of Zn cations or S anions drives the oriented attachment of ZnS nanocrystals (NCs) along this direction via electrostatic (or dipole) interaction. The ultrathin ZnS nanowires show intrinsic ferromagnetism at room temperature and other unusual properties related to its unique nature, such as large anisotropic lattice expansion, large blue-shift of UV–vis absorption band of the excitation, and photoluminescence spectrum of the exciton band edge. First-principles DFT computation results show that Zn vacancies can induce intrinsic ferromagnetism in these undoped ZnS NWs. The main source of the magnetic moment arises from the unpaired 3p electrons at S sites surrounding the Zn vacancies carrying the magnetic moment ranging from 0.26 to 0.66 μ_B . Calculated results indicate that the magnetic moment of the ultrathin ZnS NWs can be increased by increasing the Zn vacancy concentration without significant energy cost. The calculated magnetization value (1.96 or 0.40 emu/g for Zn vacancies on the surface of NWs or inside, respectively) by $\text{Zn}_{53}\text{S}_{54}$ supercell model is larger than our experimental value (0.12 emu/g at 1.8 K and 0.05 emu/g at 300 K), but the ferromagnetic result is qualitatively in agreement.



INTRODUCTION

The ultrathin nanowires (NWs) with diameter down to atomic level (<3 nm) locate at the gap of nanomaterials and molecules. There is a vast field of opportunity between these two worlds if we can couple molecular properties, like monodispersity, with the quantum size effects of nanoscale materials.¹ In recent times, the unprecedented structures of ultrathin NWs have been predicted by theory,² such as tube-like architecture and possible chirality to the nanowires,³ and, at the same time, some unique properties⁴ have been reported; among them, the ferromagnetism of the ultrathin semiconductor NWs including doping with transition metal atoms or intrinsic ferromagnetism is especially interesting because it joins both features of semiconductors and magnetic materials into a single nanoparticle, which should avoid the continuous transfer of information between semiconductors (usually used as a microprocessor) and magnetic materials (usually used as a memory) leading to faster and cheaper devices, and it combines the magnetic properties of materials with a low dimensionality of nanowires. Such synergy provides both nanoscale lateral dimensions, which are extremely beneficial for miniaturization of devices, and usually enhances physical properties due to the

strong confinement effect and the shape anisotropy. It is especially desirable to have magnetic ultrathin ZnS NWs without doping with transition-metal atoms because, in addition to device application, it possesses some ultra advantages for biomedical applications; that is, the absence of transition metal atoms may prevent the formation of dangerous free radical.

In the past two decades, one-dimensional inorganic nanostructures including semiconductor heterostructures,⁵ due to their broad range of potential applications, have been intensively investigated.⁶ Yet the diameter of the nanowires reported in the literature usually locates in the range of 5–100 nm,⁷ while that of diameter < 3 nm is quite rare so far.⁸ It is a fundamental challenge in the production of uniform ultrathin nanowires with diameter below 3 nm or even down to one unit cell limit, due to the increased difficulty to control the growth at such an atomic level. Several examples of ultrathin nanowires have been reported, such as Au,^{9,10} Ag,¹¹ Pt,⁴ⁱ Bi₂S₃,¹² Cu₂S,¹³ Sb₂S₃,¹⁴ TiO₂,¹⁵ CdS,¹⁶ EuOF,^{4h} and ZnS,^{17,18} but the spectrum of ultrathin NWs is quite

Received: June 6, 2011

Published: August 26, 2011

limited and the formation mechanism is still unclear. Also, the phase structure of NWs cannot be controlled, and the quality of the single crystalline NWs is not good enough, so the PL emission is relative to the defects and surface state. It is urgent to extend the spectrum of the ultrathin NWs for creating novel functional materials and for further understanding the formation mechanism. To this end, it is needed to exploit an efficient controlled synthesis method.

Here, we report a simple and catalyst-free one-step reaction for the synthesis of highly uniform ultrathin ZnS single crystal NWs with good quality and aspect ratio up to 5000. These nanowires are as thin as several unit cells of the ZnS crystal with hexagonal phase structure. An oriented attachment mechanism is suggested. The ZnS nanowires exhibit some unusual properties related to its unique structure, such as large anisotropic lattice expansion, photoluminescence of exciton band edge, and ferromagnetic behavior at room temperature. First-principles DFT computation was completed. The results show that wurtzite ultrathin ZnS NWs with zinc vacancies are ferromagnetic, while perfect single crystal ZnS NWs are nonmagnetic. Furthermore, the contribution to the magnetic moment may mainly come from the three S atoms that are nearest neighbor to the Zn vacancy.

EXPERIMENTAL SECTION

Chemicals. $\text{ZnSO}_4 \cdot 7\text{H}_2\text{O}$, NaOH, *n*-heptane, CHCl_3 , CS_2 , methanol, *n*-dibutylamine, and ethanol employed in this research are commercially available analytical-grade products. Dodecylamine and triphenyl phosphine were obtained from Aldrich (>98%). All reagents were used without further purification.

Synthesis of Zn(dbdc)₂ Precursor. This precursor was prepared according to the reported method.^{5c,19} For the synthesis of the $\text{Zn}(\text{S}_2\text{CN}^n\text{Bu}_2)_2$, $\text{Zn}(\text{dbdc})_2$, NaOH (2.64 g), and *n*-dibutylamine (11 mL) were added to methanol (80 mL) cooled in an ice water bath. Next, CS_2 (3.96 mL) was added into the above mixture dropwise. This yellow solution was mixed with an aqueous solution of ZnSO_4 (80 mL) containing 9.5 g of $\text{ZnSO}_4 \cdot 7\text{H}_2\text{O}$ and stirred vigorously for at least 3 h. The product was separated by filtration, washed with water several times, and dried under a vacuum at room temperature.

Synthesis of ZnS Ultrathin Nanowires. The synthesis of ZnS ultrathin nanowires was accomplished by directly thermolysis of $\text{Zn}(\text{dbdc})_2$ precursor in the mixture of organoamine and organophosphine. Typically, 60 mg of $\text{Zn}(\text{dbdc})_2$ was added to the mixture of dodecylamine (4 g) and triphenyl phosphine (PPh_3 , 1.5 g), then heated to 280 °C at a rate of 8 °C min^{-1} in a round-bottom flask under a nitrogen flow, and kept at this temperature for 20–180 min. The ZnS nanocrystals were precipitated using ethanol as a bad solvent, collected by centrifuging, washed by *n*-heptane and CHCl_3 several times, respectively, and dried under a vacuum. The obtained nanocrystals were used for further characterization.

Control Experiment with Dodecylamine Alone as Surfactant and Solvent. 60 mg of $\text{Zn}(\text{dbdc})_2$ was added to dodecylamine (4 g), then heated to 280 °C with a rate of 8 °C min^{-1} in a round-bottom flask under a nitrogen flow, and kept at this temperature for 1 h. The remaining procedures are the same as that in the synthesis of ZnS ultrathin NWs.

Control Experiment with PPh_3 Alone as Surfactant. 60 mg of $\text{Zn}(\text{dbdc})_2$ was added to the mixture of PPh_3 (1.5–0.3 g) and octadecene (4 g), then heated to 280 °C at a rate of 8 °C min^{-1} in a round-bottom flask under a nitrogen flow, and kept at this temperature for 1 h. The remaining procedures are the same as that in the above case.

Inductively Coupled Plasma (ICP) Emission Spectrometer. The sample (5.0 mg) was completely dissolved in 1 mL of 6 M HCl

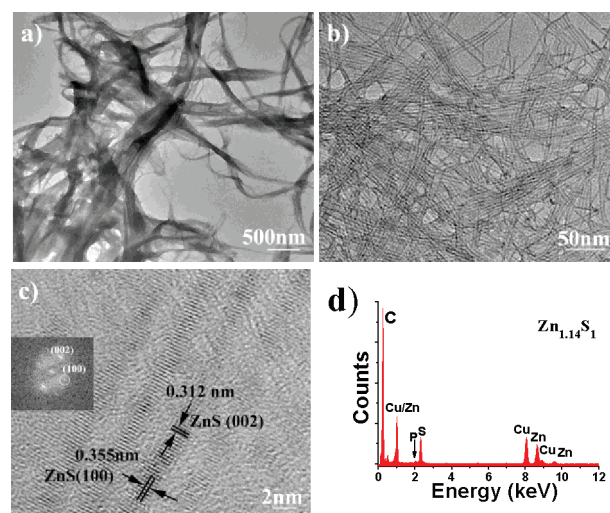


Figure 1. (a,b) TEM images of the as-prepared ZnS nanowires. (c) HRTEM image of ZnS nanowires. Inset in panel (c) is the fast Fourier transformation (FFT) pattern of the single nanowire. (d) The EDS spectrum of the ZnS nanowires: the copper and carbon signals come from the copper grid coated by carbon film, while phosphorus comes from the capping agent on the surface of ZnS nanowires.

aqueous solution, and then transferred into a 50 mL volumetric flask for ICP measurements.

Computation. First-principles DFT computations were performed using the plane-wave pseudopotential technique with the projector-augmented wave (PAW) to model the ion-electron interaction as implemented in the Vienna ab initio simulation package (VASP).

Characterization. The X-ray powder diffraction (XRD) patterns were recorded on an X'Pert diffractometer (Panalytical) with Cu K α radiation ($\lambda = 1.54060$ Å) at 45 kV, 40 mA. Accumulation time for each sample was 20 min. XRD samples were drop-casted out of CHCl_3 and showed no changes after the XRD measurements in the atmosphere. High-resolution transmission electron microscopy (HRTEM) and energy-dispersive X-ray spectra (EDS) were performed on a JEOL-2100 with accelerating voltage of 200 kV. TEM samples were prepared by drop-casting dispersion onto copper grids covered by carbon film. Fourier transform (FFT) algorithms were performed using free software, Digital-Micrograph. X-ray photoelectron spectra (XPS) were collected with a Thermo Fisher Scientific K-alpha spectrometer. The optical properties were analyzed via a Lambda-35 UV–vis spectrometer and a 48000DSCF photoluminescence spectrometer. Crystal structure model was simulated using software Diamond. Magnetic property measurements were performed using a Quantum Design MPMS XL-7 superconducting quantum interference device (SQUID). The magnetic moment M was measured as a function of applied magnetic field H at room temperature ($T = 300$ K) and low temperature ($T = 1.8$ K).

RESULTS AND DISCUSSION

ZnS Ultrathin Nanowires. The ultrathin nanowires were obtained by thermolysis of the precursor $\text{Zn}(\text{S}_2\text{CN}^n\text{Bu}_2)_2$ in the mixed solvent of organoamine and triphenyl phosphine. Figure 1 shows typical transmission electron microscopy (TEM) images of the as-obtained product with different magnifications. As seen in Figure 1a, the product is composed of many fiber-like structures. From the higher magnification image (Figure 1b), it can be clearly seen that these fiber-like structures are actually composed of many well-defined, uniform, ultrathin nanowires of ~ 2.0 nm width and several micrometers (up to 10 μm) length. The dia-

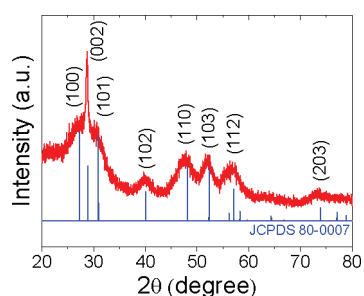


Figure 2. XRD pattern of the ultrathin ZnS NWs. The standard XRD pattern of hexagonal (JCPDS 80-0007) is also shown for comparison.

meter is well below the exciton Bohr radius of ZnS (2.5 nm).¹⁸ The ultrathin nanowires display remarkable diameter uniformity and will melt under an e-beam irradiation for a little longer time. The corresponding EDS analysis (Figure 1d) reveals that the nanowires contain zinc and sulfur with a nearly 1:1 atomic ratio for Zn to S, as well as the presence of phosphorus.

The HRTEM (Figure 1c) image of the ZnS nanowires shows the nature of single crystalline with lattice fringes of 0.312 and 0.355 nm corresponding to the spacings of (002) and (100) lattice planes of hexagonal ZnS, respectively, and the preferential growth direction of the nanowires is along the *c* axis. An obvious lattice expansion up to 8.6% ((0.355–0.327 nm)/0.327 nm) has been observed for the lattice spacing of (100) facet (0.355 nm), which is much bigger than that of the bulk crystalline lattice (0.327 nm). Yet the lattice spacing of the (002) plane (0.312 nm) agrees well with the standard value (0.309 nm), indicating the anisotropic feature of the lattice expansion. It is reasonable because the size of (100) facet direction is only 2 nm, while the length of nanowires along the [002] direction is micrometer-scale. Ultrathin single crystal ZnS nanowires up to 10 μm long are reported for the first time.

The crystal structure of the ultrathin ZnS NWs was examined by X-ray diffraction. The diffraction pattern in Figure 2 clearly demonstrates that the nanowires are pure hexagonal ZnS (JCPDF 80-0007, *a* = 0.3777 nm, *c* = 0.6188 nm). The crystallographic parameters calculated from XRD pattern are *a* = 0.3810 nm and *c* = 0.6214 nm. The apparent broadening of the diffraction peaks is indicative of the small size of the ZnS nanocrystals. The (002) diffraction peak, on the other hand, exhibits a relatively narrow peak width, which implies the formation of ZnS ultrathin NWs with a preferred growth orientation along the direction of (002) plane, the *c* axis direction of the hexagonal crystal structure.⁸ This is consistent with HRTEM analysis. Comparing the XRD pattern with the standard one, all diffraction peaks shift to lower angles, except the (002) peak. This suggests the obvious lattice expansion, which also agrees well with the HRTEM observation.

Growth Mechanism. The key point for preparation of ultrathin nanowires is to coerce the nanowires growing preferentially in one direction, while the growth along the other two directions is completely halted. Usually, it is accomplished by using template or using surfactants to reduce surface energy.¹ Another route is assembling the preformed nanocrystals, that is, oriented attachment.^{1,17} To gain insight into the formation mechanism of ultrathin ZnS NWs, the formation process of nanowires was traced with reaction time. TEM images of ZnS samples acquired at various reaction stages are shown in Figure 3. ZnS nanocrystals with diameter of about 2 nm (equivalent to several unit cells) are first

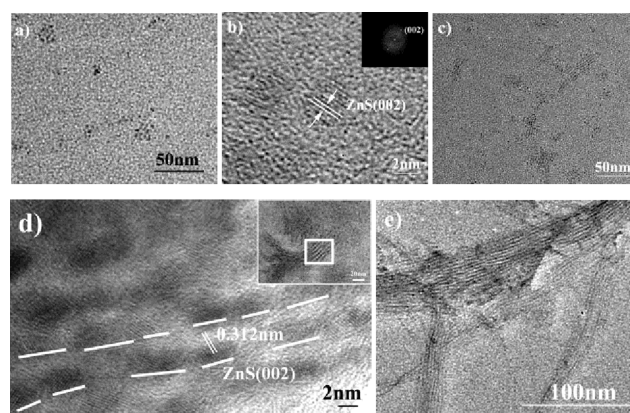


Figure 3. (a) TEM image of the sample extracted when the reaction is heated to 120 °C. (b) HRTEM image of the sample in (a); the inset of (b) is the corresponding FFT pattern of the nanocrystal. (c) TEM image of that at 180 °C. (d) HRTEM image of the sample in (c) and indicated by a white square in the inset, and (e) TEM image of that at 250 °C.

formed when the reaction system is heated to 120 °C at the rate of ~8 °C/min (Figure 3a). The HRTEM image (Figure 3b) shows that ZnS NCs are ellipse-like nanostructures with wurtzite structure, and the long axis is along the *c* axis. With further increasing of the reaction temperature to 180 °C at the same rate, some loosely associated aggregates begin to form (Figure 3c,d) (Figure S1, see the Supporting Information). This necklace-like embryo of nanowires is composed of ZnS NCs. The connection points between nanocrystals in the embryo of nanowires can be clearly seen (Figure S1, see the Supporting Information). The ultrathin NWs are formed when the reaction temperature increased up to 250 °C (Figure 3e).

On the basis of these TEM and HRTEM experimental observations, an oriented attachment mechanism of ultrathin nanowire formation is suggested (Figure 4a), in which a necklace-like nanostructure is a key and feature intermediate.²⁰ First, the precursor species were thermolyzed with the assistance of organoamine and triphenyl phosphine^{20a} to form ZnS ellipse-like nanocrystals dominated by {001} basal facets and {100} side facets. The {001} lattice planes (basal facets of ZnS ellipse-like NCs) are polar planes composed of S anions or Zn cations (Figure 4c). This makes each ZnS NC a stronger dipole along the [001] direction (stronger than that of cubic ZnS NCs along the [111] direction, Figure 4b), which drives the oriented attachment of ZnS NCs along this direction. Further ripening makes the loosely associated prewire aggregates evolve into a single crystal, whereas there is no dipole (or electrostatic) interaction in the direction of (100) planes of ZnS NCs, which, combined with the heavy covering of the surfactants, completely prevents growth of ZnS NCs along the direction of (100) planes and ensures the formation of ultralong ultrathin nanowires.

The formation of the ZnS ultrathin nanowires is highly dependent on the composition ratio of organophosphine and organoamine. Control experiments show that when dodecylamine alone is used as solvent and surfactant, the reaction product is shorter nanorods with cubic phase structure, and the long axis is parallel to the direction of (111) plane of ZnS nanorods. When PPh₃ alone was used as solvent and surfactant, only spherical nanoparticles were obtained because the very strong binding ability of PPh₃ leads to near isotropic growth. XRD data of the spherical nanoparticles obtained with PPh₃ alone exhibit a very broad peak

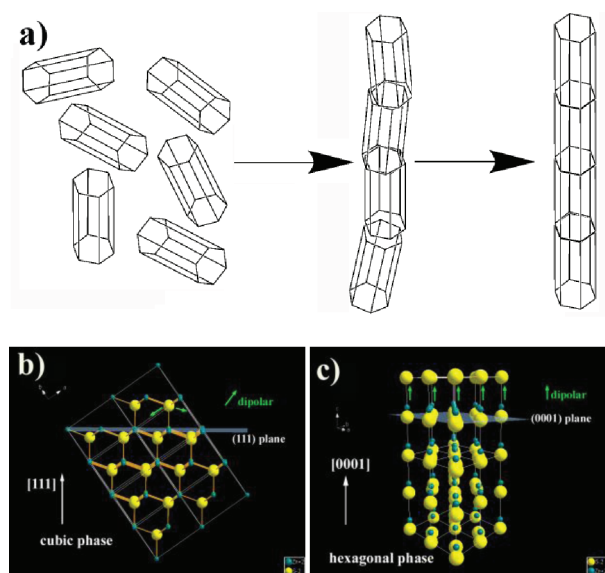


Figure 4. (a) The formation scheme of ZnS ultrathin nanowires through oriented attachment mechanism. (b,c) Crystal structures of (b) cubic and (c) hexagonal phase ZnS. The difference between cubic and hexagonal phase ZnS is the stacking mode of the atomic planes. That of the cubic phase is a stacking of ABCABC parallel to the close packing plane (111), while that of wurtzite is a stacking of ABAB for {001} planes, which means that the hexagonal phase has a bigger ionic bond part, and so a stronger dipole along the [001] direction.

between 24° and 33° , which might be attributed to the hexagonal phase ZnS most probably (Figure S2, see the Supporting Information). There is an optimum ratio between dodecylamine and PPh_3 . At that ratio, formed ellipse-like ZnS NCs all are hexagonal phase structure with {001} basal plane, and the growth along the direction of (100) planes is completely prevented, which is the key factor leading to the formation of ZnS ultrathin NWs via oriented attachment growth. X-ray photoelectron spectra (XPS) show that elements N and P coexist on the surface of ZnS ultrathin nanowires, which evidence the coordination of two surfactants on the surface of ZnS (Figure S3, see the Supporting Information). In addition, it reveals the ZnS ultrathin nanowires have a composition of $\text{Zn}_1\text{S}_{1.3}$.

To gain insight into the role played by PPh_3 , a series of control experiments were conducted (Table S1, see the Supporting Information). First, increasing the weight ratio of organophosphine to dodecylamine from the optimum one has no detectable influence on the formation of ultrathin nanowires, while gradually decreasing that weight ratio from 0.37 to 0.15 gradually decreases the yield of ultrathin nanowires; that is, ultrathin nanowires and NCs coexist. When the weight ratio is further decreased, the ultrathin ZnS nanowires become a minor component and completely disappear in the end. At the same time, the NCs become nanorods with cubic phase structure. Its diameter is about 4 nm. The average length is 8 nm (Table S1, Figure S4, see the Supporting Information). These cubic ZnS nanorods do not attach along the [111] direction likely due to the relatively weak dipole interaction (Figure 4b).

These experimental results exhibit that organophosphine plays an important role in the formation of ultrathin ZnS NWs with wurtzite structure. With the PPh_3 concentration below the critical value, ZnS NCs with cubic phase structure will form. It is well-known that the structural transformation between the zinc blend

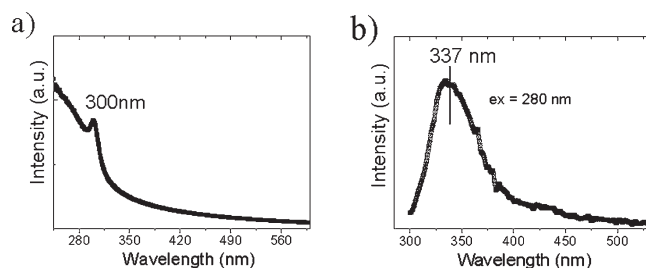


Figure 5. (a) UV-vis absorption spectrum and (b) photoluminescence spectrum of ZnS ultrathin nanowires in CHCl_3 .

and wurtzite phases depends on the reaction conditions and the components of the reaction solutions in the synthesis of binary II-VI and III-V semiconductor NCs.^{21–24} Trioctylphosphine, trioctylphosphine oxide, and tetradecylphosphonic acid can also be used as surfactant instead of PPh_3 for the preparation of ZnS ultrathin nanowires.

Another series of control experiments were conducted with changing the weight ratio of organophosphine to the ZnS precursor at the optimum weight ratio of organophosphine to dodecylamine. The results show that increasing the weight ratio of organophosphine to the precursor has no detectable influence on the formation of ultrathin nanowires, while by decreasing the weight ratio, the yield of ultrathin nanowires decreases and NCs form at same time. At last, ultrathin nanowires all disappear, and ZnS nanorods become the only product (Table S1, Figure S4, see the Supporting Information) because the stronger binding ability of organophosphine makes the weight ratio of the two surfactants in the reaction solution decrease from the optimum to below the critical value. The trend of variation is the same as that in the case of changing the weight ratio of the two surfactants. This further evidences that the organophosphine promotes the formation of hexagonal phase structure ZnS NCs with polar basal plane (001) and strongly binds on the surface of ZnS ellipse-like NCs to prevent the growth along the direction of the (100) plane, but it does not block the dipole interaction along the direction of (001) plane, which are the important factors for the oriented attachment of ZnS NCs and the formation of ZnS ultrathin ultralong nanowires.

Optical Properties. To inspect the quantum confinement effect of ultrathin ZnS nanowires, UV-vis absorption and PL spectra were measured. Figure 5a shows the UV-vis absorption spectrum of the ultrathin ZnS nanowires. The absorption band located at 300 nm (4.13 eV) has blue-shifted significantly from the bulk band gap (2.77 eV (448 nm) for hexagonal ZnS nanowires)²⁵ due to very strong two-dimensional quantum confinement effects. The sharp absorption peak provides further evidence that the diameter of nanowires is uniform along the length. The PL spectrum of the ultrathin ZnS nanowires in CHCl_3 solution at room temperature shows (Figure 5b) a strong UV emission band centered at 337 nm, which is attributed to excitonic emission. A remarkable Stokes shift of 30 meV is observed due to electron-phonon coupling. There is no emission band of the defects and trapping state in the PL spectrum, which usually centers at around 500 nm after being excited at 280 nm. It further evidence that the concentration of defects is very low and the quality of the ZnS single crystal ultrathin nanowires prepared here is good enough.

Magnetic Properties. The magnetic behavior of the synthesized ZnS ultrathin nanowires is investigated by superconducting

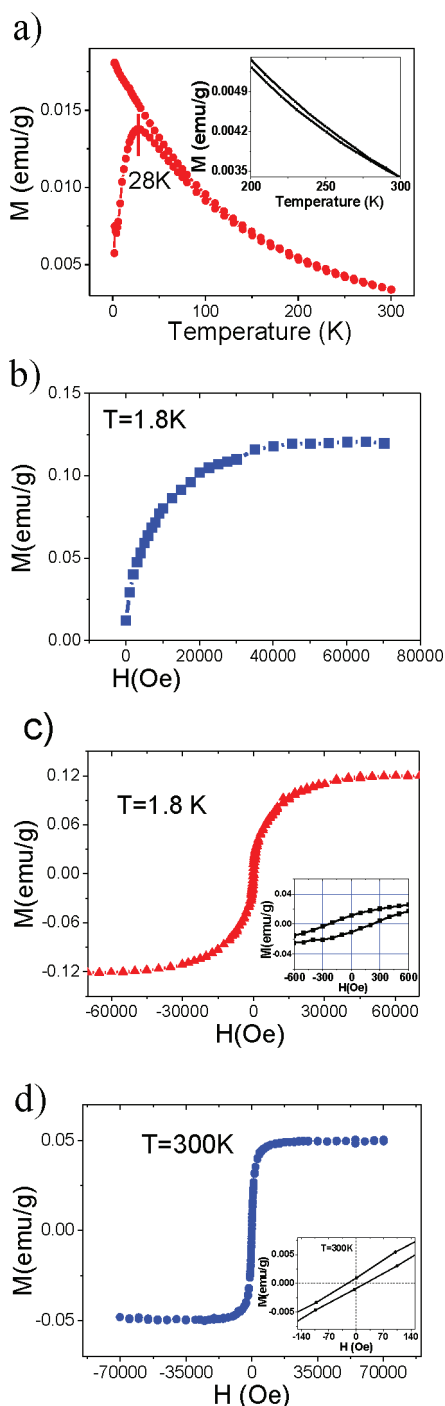


Figure 6. (a) Temperature-dependent magnetization of ZnS ultrathin nanowires obtained by zero-field cooling and field cooling in an external field of 100 Oe. (b–d) Field dependence of the magnetization of ZnS ultrathin nanowires at (b,c) 1.8 K and (d) 300 K after subtracting the high-field diamagnetic contribution. The insets in (a), (c), and (d) are the corresponding magnified figures.

quantum interference device (SQUID). Figure 6a shows the magnetization (M) versus temperature (T) curves under zero magnetic field cooling (ZFC) and field cooling (FC) at applied field of 100 Oe. A divergence of ZFC and FC curves is observed around 300 K (the inset of Figure 6a). The M – H curves of ZnS ultrathin nanowires in the applied field range of 0–70 kOe are

shown in Figure 6b–d. The raw data were corrected by subtracting the diamagnetic contribution from the high field regions. The magnetization approaches saturation at the applied fields of about 40 kOe at 1.8 K (Figure 6b,c) and 15 kOe at 300 K (Figure 6d), respectively. The saturation magnetizations (M_s) are up to 0.12 emu/g at 1.8 K and 0.05 emu/g at 300 K. There is an obvious hysteresis loop in the M – H plot with $H_c = 235$ Oe at 1.8 K and about 25 Oe at 300 K. These results suggest that the ZnS ultrathin nanowires show ferromagnetic feature at room temperature. The magnetic contribution from metal impurities was evaluated. The magnetic impurities in the ZnS ultrathin nanowires were determined by inductively coupled plasma emission spectroscopy (ICP). Only iron was found in the sample with 87 ppm, while other magnetic metals were below the detectable limits (Table S2, see the Supporting Information). Supposing all 87 ppm of Fe atoms in the sample form one particle of Fe_3O_4 , the contribution of the Fe impurities to M_s was calculated to be 0.008 emu/g (using $M_s = 92$ emu/g for bulk Fe_3O_4), which is much smaller than measured value of the ZnS ultrathin nanowires. Furthermore, the calculated M_s value is overestimated, and the actual contribution of magnetic impurities is much smaller than the value of 0.008 emu/g. Therefore, the magnetic behavior is the inherent nature of the ZnS ultrathin nanowires.

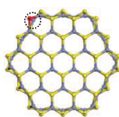
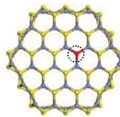
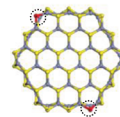
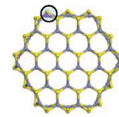
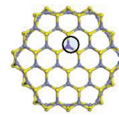
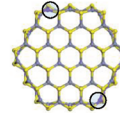
DFT Computations. It is hard to understand the origin of this kind magnetism of nonmagnetic materials. Several factors may be relative to this novel magnetism, such as defects, capping agent binding, and lattice expansion. To obtain an insight into the origin of the magnetic behavior of the ultrathin ZnS NWs, first-principles DFT computations were performed using the plane-wave pseudopotentials technique with the projector augmented wave to model the ion–electron as implemented in the Vienna ab initio simulation package (VASP) (see the Supporting Information for details, Figure S5–7). The main results are as follows.

For Perfect Single Crystal Wurtzite ZnS Nanowire. Both spin-unpolarized and spin-polarized computations have been carried out during the optimization of ZnS nanowire. Results indicate that perfect single crystal ZnS nanowire has a nonmagnetic ground state (total magnetic moment $M_{\text{tot}} = 0$), which is consistent with previous reports.²⁶ The spin-unpolarized band structure of perfect ZnS nanowire is shown in Figure S8 (see the Supporting Information). It can be seen that the ZnS nanowire is semiconducting with a direct band gap of 2.75 eV at the Γ point. Because of the quantum confinement effect in one-dimensional (1D) perfect ZnS nanowire, the band gap increased about 0.30 eV in comparison with that (2.45 eV) of three-dimensional (3D) bulk wurtzite crystal. By adding 1.25 eV (systematic derivation of the GGA+U method, see the Supporting Information for details) to the raw direct band gap of perfect ZnS nanowire, the corrected band gap E_g of 4.00 eV is obtained. The calculated absorption wavelength λ_o of ZnS nanowire by using the formula $\lambda_o = 1240/E_g$ is 310 nm, which is very close to our experimental value of 300 nm and indicates that our constructed ZnS nanowire model is rational.

The electronic structure of the perfect ZnS nanowire can be seen from the total densities of states (DOSs) plotted in Figure S9a (see the Supporting Information), where the spin-up and spin-down DOSs are completely symmetric and the energy gap is located around the Fermi level, which indicate again that this system is nonmagnetic and semiconducting.

For Defective Wurtzite ZnS Nanowire. Supposing one vacancy of S or Zn on the surface and inside the supercell containing 54 f.u. of ZnS, respectively (Table 1 (a_1), (b_1) and (a_2), (b_2))), this led

Table 1. Summary of the First-Principles DFT Computations^a

	<i>S</i> vacancy $Zn_{54}S_{54-x}$ ($1 \leq x \leq 2$)			<i>Zn</i> vacancy $Zn_{54-y}S_{54}$ ($1 \leq y \leq 2$)		
						
	a_1	a_2	a_3	b_1	b_2	b_3
	$x = 1$ (1.85 %)	$x = 1$ (1.85 %)	$x = 2$ (3.70 %)	$y = 1$ (1.85 %)	$y = 1$ (1.85 %)	$y = 2$ (3.70 %)
E_f (eV)	6.54	7.58	6.54	3.88	4.52	3.89
M_{tot} (μ_B)	0.00	0.00	0.00	1.84	0.38	3.69
M_{tot} (emu/g)	0.00	0.00	0.00	1.96	0.40	3.94

^a The schematic representation of the vacancy configurations in (a_1 – a_3) $Zn_{54}S_{54-x}$ ($1 \leq x \leq 2$) and (b_1 – b_3) $Zn_{54-y}S_{54}$ ($1 \leq y \leq 2$) nanowire supercell; formation energy of the vacancies (E_f) and total magnetic moment per supercell (M_{tot}) for different vacancy concentrations and configurations of $Zn_{54}S_{54-x}$ ($1 \leq x \leq 2$) and $Zn_{54-y}S_{54}$ ($1 \leq y \leq 2$) nanowire supercell. The yellow and grey spheres represent S and Zn atoms, respectively. The red and purple spheres show the sites where the atoms are removed to generate S and Zn vacancies, respectively.

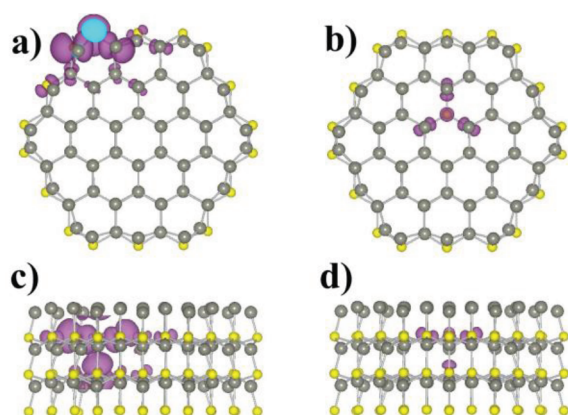


Figure 7. Spatial spin density distribution (up–down) of Zn-defective ZnS nanowires $Zn_{53}S_{54}$. (a) Top view and (c) side view of Zn vacancy at the surface, (b) top view and (d) side view of Zn vacancy in the core. The yellow and gray spheres represent S and Zn atoms, respectively. It suggests that the Zn vacancies on the nanowire surface give main contribution to the ferromagnetism of the ultrathin nanowire.

to a ZnS super cell containing a sulfur or zinc vacancy concentration of 1.85%. The calculated vacancy formation energies of S and Zn on the surface are 6.54 and 3.88 eV, respectively, while those inside are 7.58 and 4.52 eV (Table 1). This suggests that the energy cost to remove a S atom is much more than that for a Zn atom in the ZnS nanowire, and both S and Zn vacancies prefer to reside on the surface because there is less number of bonds that need to be broken, similar to the situation in ZnO nanowire.²⁷ Calculations on the ZnS nanowire supercells containing two S or Zn vacancies are also carried out, respectively, to investigate the influence of vacancy concentration on the electronic and magnetic properties of the nanowire (Table 1 (a_3), (b_3)). The results are summarized in Table 1.

From Table 1, we can see that the $Zn_{53}S_{54}$ supercell (surface Zn vacancy) carries a total magnetic moment of $1.84 \mu_B$, while that of $Zn_{54}S_{53}$ is $0 \mu_B$. This indicates that Zn vacancy can induce ferromagnetism in the ultrathin ZnS NWs, while S vacancy (irrespective of where it lies) cannot even though the S vacancy

concentration is increased from 1.85% to 3.70%. Moreover, the computation results further indicate that the magnetism of the ZnS NWs increased from 1.84 to $3.69 \mu_B$ with the surface Zn vacancy concentration increasing from 1.85% to 3.70%. At the same time, the Zn vacancy formation energy changes only about 0.01 eV. Thus, the magnetic moments of defective ZnS nanowires can be raised by increasing the Zn vacancy concentration without significant energy cost.

To further examine the origin and distribution of the ferromagnetism, the self-consistently local magnetic moment and spin density distribution calculations were performed (Figure 7). The results show that the contribution to magnetism mostly comes from the nearest neighboring three S atoms around the Zn vacancy. Take the $Zn_{53}S_{54}$ supercell as an example, the local magnetic moments on the three nearest-neighbor S sites of the Zn vacancy are 0.27 , 0.68 , and $0.63 \mu_B$, respectively, and mainly originate from the p orbital of S atoms (0.26 , 0.66 , and $0.61 \mu_B$), while those of Zn atoms nearest to the Zn vacancy are negligible, which is similar to the Zn-defective ZnO nanowires.²⁶ From Table 1, we also note that the formation energy of Zn vacancy inside the nanowire is about 0.64 eV higher than that on the surface and the Zn vacancy inside the NW leads to weaker ferromagnetism ($M_{tot} = 0.38 \mu_B$), which is different from the ZnO nanowire.²⁶ It indicates that the Zn vacancy prefers to reside on the nanowire surface and give important contribution to the ferromagnetism of the ultrathin nanowire.

Although the ultrathin nanowires are heavily covered by surfactants, the nucleophilic surfactants (triphenyl phosphine and dodecylamine) are mainly bonded on the metal sites through their coordination atoms, N or P, and would have less effect on the sulfur atoms around the Zn vacancies. Their effect on the magnetism induced by Zn vacancies is probably limited. In addition, although the formation energy of Zn vacancies inside the nanowires is bigger than that on the surface, it does not exclude the formation of the inner vacancies at all; only the amount is less than that on the surface. The inner Zn vacancies would also offer some extent contribution to magnetism of the ultrathin ZnS nanowires. Combined together, it is reasonable that the Zn vacancies induce the magnetism of the ultrathin ZnS nanowires.

However, it is difficult to determine the amount of Zn vacancies by experiments; XPS data showing the elemental composition

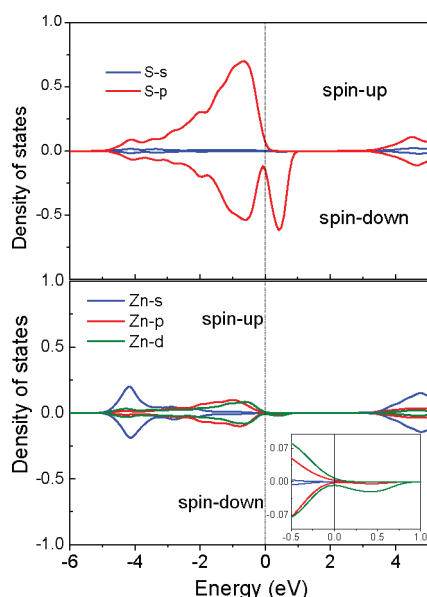


Figure 8. Partial DOSs of sulfur (upper panel) and Zn (bottom panel) atoms located around Zn vacancy. It can be seen that the unpaired spins mainly arise from the nearest-neighbor S atoms of the Zn vacancies.

($Zn_{1.3}S_{1.3}$) of the as-grown ZnS nanowires may give some indication for the presence of Zn vacancies. On the other hand, there is more sulfur in the molecular precursor ($Zn(dbdc)_2$) than the stoichiometric ratio in ZnS, which would be of benefit to form Zn vacancies.

To investigate the changes in electronic structure and magnetic properties resulting from Zn vacancies, the total DOSs and partial DOSs of Zn and S atoms for configuration b_1 shown in Table 1 were shown in Figure S9a–c (see the Supporting Information) and Figure 8. It can be seen that total DOSs at the Fermi level are significant difference between defective $Zn_{53}S_{54}$ and perfect $Zn_{54}S_{54}$. The Zn vacancy induces an asymmetric DOSs for spin-up and spin-down (Figure 8), that is, spin polarization at the VBM (valence band maximum). The partial DOSs of nearest-neighbor four Zn atoms and three S atoms around the Zn vacancy in the defective nanowire ($Zn_{53}S_{54}$) supercell were plotted in Figure 8, respectively, which clearly showed that the main contribution to the observed magnetic moment comes from the S 3p orbitals, while one from the Zn atoms was quite little, which is in agreement with foregoing local magnetic moment calculations and the spin density distribution calculation results (Figure 7). Thus, it is clear that the presence of Zn vacancies in ZnS nanowire leads to the spin polarization of S 3p orbitals and to the introduction of new states near the Fermi level, which is relative to the atomic properties of sulfur with two unpaired 3p electrons. Although the calculated magnetization value of the ultrathin ZnS NWs is larger than our experimental one, the ferromagnetic result is qualitatively in agreement. The calculated value may be improved by decreasing the concentration of Zn vacancy in supercell model. A low vacancy concentration is in agreement with our experimental results shown in HRTEM, UV–vis absorption spectrum, and PL spectrum. Yet due to the tremendous computation time, we cannot do it at present.

The computational results further indicate that the energy of the spin-polarized state (i.e., ferromagnetic state) is 31.5 meV lower than that of spin-unpolarized states (i.e., nonmagnetic state) of the defective ultrathin ZnS NWs (Table 1 (b_1)). The energy

difference (31.5 meV) is bigger than the thermal energy corresponding to the room temperature. Therefore, the ferromagnetic state could be stable at room temperature, which is in agreement with our experimental results.

The most recent and outstanding works showed that the magnetism in nanostructures of nonmagnetic materials are not exclusively related to the presence of the defects but also contributed by the interaction between surface atoms and capping agents.²⁸ It has been demonstrated that the capping of molecules containing N or S on ZnO or noble metal nanoparticles would alter their electronic configuration and induce magnetism. Although capping agents interacting with the surface atoms will change the electronic states and lead to exotic magnetic behavior, the magnetization induced by the surfactants binding is weaker, only 10^{-2} – 10^{-3} emu/g, which is much less than our experimental data. On the basis of these, we consider that the contribution by surfactant binding might be neglectable. The lattice expansion will also affect the electronic states, and therefore magnetism, but we may conjecture that it will be weaker than that induced by vacancies because the formation of the vacancies involves chemical bond breaking, which creates unpaired electrons, while lattice expansion only lengthens bond length. The exact contribution of these factors to the magnetism remains obscure because of the complexity of the research system, and further studies are expected.

CONCLUSIONS

Uniform ZnS ultrathin single crystal nanowires with diameter of 2 nm were fabricated in one-pot reaction using a mixture of dodecylamine and triphenyl phosphine as the solvent and capping agent. The ultrathin ZnS nanowires are formed through orientated attachment of ZnS NCs, and the phase structure can be controlled. It is not accessible with previous synthetic protocols. The ultrathin nanowires exhibit a ferromagnetic behavior at room temperature and a stronger quantum confinement effect. The first-principles DFT computations were completed, and the results show that the ZnS ultrathin NWs with Zn vacancies ($Zn_{53}S_{54}$ supercell) have a ferromagnetic ground state, while that with S vacancies ($Zn_{54}S_{53}$ supercell) is nonmagnetic. The contribution to magnetism may mostly come from three nearest-neighbor S sites surrounding the Zn vacancy, of which the p orbital of S atoms offers the main part, whereas the contribution of Zn atoms nearest to the Zn vacancy is negligible. The Zn vacancy inside the ZnS NWs has a formation energy of 0.64 eV higher than that on the surface and induces a weaker ferromagnetism ($M_{tot} = 0.38 \mu_B$). The ultrathin ZnS NWs with intrinsic ferromagnetic are especially desirable for miniaturizing devices and biomedical application. This simple synthetic strategy may have a promising application in the study of semiconductor nanowires with a strong quantum confinement effect. Meanwhile, these well-defined building blocks could offer more opportunities for investigating their collective properties, as well as open a door for other important technological applications.

ASSOCIATED CONTENT

S Supporting Information. TEM and HRTEM images of ZnS ultrathin nanowires, XPS spectra, ICP results, XRD of the product with PPh₃ as surfactant, crystal structure of cubic and hexagonal ZnS, control experiments, and the corresponding

results. This material is available free of charge via the Internet at <http://pubs.acs.org>.

AUTHOR INFORMATION

Corresponding Author

zhengxu@nju.edu.cn

ACKNOWLEDGMENT

Financial support from the National Major Basic Research Program (973 program 2007CB936302) and the National Natural Science Foundation of China under major project no. 90606005 is greatly appreciated.

REFERENCES

- (1) Cademartiri, L.; Ozin, G. A. *Adv. Mater.* **2009**, *21*, 1013–1020.
- (2) Gulseren, O.; Ercolessi, F.; Tosatti, E. *Phys. Rev. Lett.* **1998**, *80*, 3775–3778.
- (3) Oshima, Y.; Koizumi, H.; Mouri, K.; Hirayama, H.; Takayanagi, K.; Kondo, Y. *Phys. Rev. B* **2002**, *65*, 121401–1–4.
- (4) (a) Pascual, J. I.; Mendez, J.; Gomezherrero, J.; Baro, A. M.; Garcia, N.; Landman, U.; Luedtke, W. D.; Bogachek, E. N.; Cheng, H. P. *Science* **1995**, *267*, 1793–1795. (b) Arutyunov, K. Y. *Phys. C* **2008**, *468*, 272–275. (c) Dresselhaus, M. S.; Chen, G.; Tang, M. Y.; Yang, R. G.; Lee, H.; Wang, D. Z.; Ren, Z. F.; Fleurial, J. P.; Gogna, P. *Adv. Mater.* **2007**, *19*, 1043–1053. (d) Teng, X. W.; Han, W. Q.; Ku, W.; Hucker, M. *Angew. Chem., Int. Ed.* **2008**, *47*, 2055–2058. (e) Zhao, X. Y.; Wei, C. M.; Yang, L.; Chou, M. Y. *Phys. Rev. Lett.* **2004**, *92*, 236805–1–4. (f) Boukai, A. I.; Bunimovich, Y.; Tahir-Kheli, J.; Yu, J. K.; Goddard, W. A.; Heath, J. R. *Nature* **2008**, *451*, 168–171. (g) Hochbaum, A. I.; Chen, R. K.; Delgado, R. D.; Liang, W. J.; Garnett, E. C.; Najarian, M.; Majumdar, A.; Yang, P. D. *Nature* **2008**, *451*, 163–167. (h) Du, Y. P.; Zhang, Y. W.; Yan, Z. G.; Sun, L. D.; Yan, C. H. *J. Am. Chem. Soc.* **2009**, *131*, 16364–16365. (i) Sun, S.; Zhang, G.; Zhong, Y.; Liu, H.; Li, R.; Zhou, X.; Sun, X. *Chem. Commun.* **2009**, 7048–7050. (j) Liu, J. W.; Zhu, J. H.; Zhang, C. L.; Liang, H. W.; Yu, S. H. *J. Am. Chem. Soc.* **2010**, *132*, 8945–8952.
- (5) (a) Cozzoli, P. D.; Pellegrino, T.; Manna, L. *Chem. Soc. Rev.* **2006**, *35*, 1195–1208. (b) Casavola, M.; Buonsanti, R.; Caputo, G.; Cozzoli, P. D. *Eur. J. Inorg. Chem.* **2008**, *6*, 837–838. (c) Zhu, G. X.; Xu, Z. *J. Am. Chem. Soc.* **2011**, *133*, 148–157. (d) Zeng, H.; Li, J.; Wang, Z. L.; Liu, J. P.; Sun, S. *Nano Lett.* **2004**, *4*, 187–190. (e) Li, Z.; Cheng, L.; Sun, Q.; Zhu, Z.; Riley, M. J.; Aljada, M.; Cheng, Z.; Wang, X.; Hanson, G. R.; Qiao, S.; Smith, S. C.; Lu, G. Q. *Angew. Chem., Int. Ed.* **2010**, *49*, 2777–2781.
- (6) Wang, F.; Dong, A.; Sun, J.; Tang, R.; Yu, H.; Buhro, W. E. *Inorg. Chem.* **2006**, *45*, 7511–7521.
- (7) Kuno, M. *Phys. Chem. Chem. Phys.* **2008**, *10*, 620–639.
- (8) Huo, Z. Y.; Tsung, C. K.; Huang, W.; Fardy, M.; Yan, R.; Zhang, X. F.; Li, Y. D.; Yang, P. D. *Nano Lett.* **2009**, *9*, 1260–1264.
- (9) (a) Lu, X. M.; Yavuz, M. S.; Tuan, H. Y.; Korgel, B. A.; Xia, Y. N. *J. Am. Chem. Soc.* **2008**, *130*, 8900–8901. (b) Xu, J.; Wang, H.; Liu, C. C.; Yang, Y. M.; Chen, T.; Wang, Y. W.; Wang, F.; Liu, X. G.; Xing, B. G.; Chen, H. Y. *J. Am. Chem. Soc.* **2010**, *132*, 11920–11922. (c) Wang, C.; Hu, Y. J.; Lieber, C. M.; Sun, S. H. *J. Am. Chem. Soc.* **2008**, *130*, 8902–8903. (d) Xu, J.; Wang, H.; Liu, C. C.; Yang, Y. M.; Chen, T.; Wang, Y. W.; Wang, F.; Liu, X. G.; Xing, B. G.; Chen, H. Y. *J. Am. Chem. Soc.* **2010**, *132*, 11920–11922.
- (10) Wang, C.; Sun, S. *Chem. Asian J.* **2009**, *4*, 1028–1034.
- (11) Hong, B. H.; Bae, S. C.; Lee, C. W.; Sukmin, J.; Kim, K. S. *Science* **2001**, *294*, 348–351.
- (12) (a) Cademartiri, L.; Malakooti, R.; O'Brien, P. G.; Migliori, A.; Petrov, S.; Kherani, N. P.; Ozin, G. A. *Angew. Chem., Int. Ed.* **2008**, *47*, 3814–3817. (b) Thomson, J. W.; Cademartiri, L.; MacDonald, M.; Petrov, S.; Calestani, G.; Zhang, P.; Ozin, G. A. *J. Am. Chem. Soc.* **2010**, *132*, 9058–9068. (c) Cademartiri, L.; Scotognella, F.; O'Brien, P. G.; Lotsch, B. V.; Thomson, J.; Petrov, S.; Kherani, N. P.; Ozin, G. A. *Nano Lett.* **2009**, *9*, 1482–1486.
- (13) Liu, Z. P.; Xu, D.; Liang, J. B.; Shen, J. M.; Zhang, S. Y.; Qian, Y. T. *J. Phys. Chem. B* **2005**, *109*, 10699–10704.
- (14) Malakooti, R.; Cademartiri, L.; Migliori, A.; Ozin, G. A. *J. Mater. Chem.* **2008**, *18*, 66–69.
- (15) Liu, C. M.; Sun, H.; Yang, S. H. *Chem.-Eur. J.* **2010**, *16*, 4381–4393.
- (16) Zhuang, Z. B.; Lu, X. T.; Peng, Q.; Li, Y. D. *J. Am. Chem. Soc.* **2010**, *132*, 1819–1821.
- (17) Deng, Z. T.; Yan, H.; Liu, Y. *Angew. Chem., Int. Ed.* **2010**, *49*, 8695–8698.
- (18) Zhang, Y. J.; Xu, H. R.; Wang, Q. *Chem. Commun.* **2010**, 46, 8941–8943.
- (19) Pan, D. C.; An, L. J.; Sun, Z. M.; Hou, W.; Yang, Y.; Yang, Z. Z.; Lu, Y. F. *J. Am. Chem. Soc.* **2008**, *130*, 5620–5621.
- (20) (a) Barnard, A. S.; Xu, H.; Li, X.; Pradhan, N.; Peng, X. G. *Nanotechnology* **2006**, *17*, 5707–5714. (b) Penn, R. L.; Banfield, J. F. *Science* **1998**, *281*, 969–971. (c) Pacholski, C.; Kornowski, A.; Weller, H. *Angew. Chem., Int. Ed.* **2002**, *41*, 1188–1191. (d) Lou, X. W.; Zeng, H. C. *J. Am. Chem. Soc.* **2003**, *125*, 2697–2704. (e) Cho, K. S.; Talapin, D. V.; Gaschler, W.; Murray, C. B. *J. Am. Chem. Soc.* **2005**, *127*, 7140–7147. (f) O'Sullivan, C.; Gunning, R. D.; Sanyal, A.; Barrett, C. A.; Geaney, H.; Laffir, F. R.; Ahmed, S.; Ryan, K. M. *J. Am. Chem. Soc.* **2009**, *131*, 12250–12257. (g) Chen, J. S.; Zhu, T.; Li, C. M.; Lou, X. W. *Angew. Chem., Int. Ed.* **2011**, *50*, 650–653.
- (21) Kim, Y. H.; Jun, Y.; Jun, B.; Lee, S. M.; Cheon, J. *J. Am. Chem. Soc.* **2002**, *124*, 13656–13657.
- (22) Li, Y. C.; Li, X.; Yang, C.; Li, Y. F. *J. Phys. Chem. B* **2004**, *108*, 16002–16011.
- (23) Yu, W. W.; Wang, Y. A.; Peng, X. G. *Chem. Mater.* **2003**, *15*, 4300–4308.
- (24) Cozzoli, P. D.; Manna, L.; Curri, M. L.; Kudara, S.; Giannini, C.; Striccoli, M.; Agostiano, A. *Chem. Mater.* **2005**, *17*, 1296–1306.
- (25) Xiong, S. L.; Xi, B.; Wang, C.; Xu, D.; Feng, X.; Zhu, Z.; Qian, Y. T. *Adv. Funct. Mater.* **2007**, *17*, 2728–2738.
- (26) Li, Y. F.; Zhou, Z.; Jin, P.; Chen, Y. S.; Zhang, S. B.; Chen, Z. F. *J. Phys. Chem. C* **2010**, *114*, 12099–12103.
- (27) Wang, Q.; Sun, Q.; Chen, G.; Kawazoe, Y.; Jena, P. *Phys. Rev. B* **2008**, *77*, 205411–1–7.
- (28) (a) Crespo, P.; Litran, R.; Multigner, M.; de la Fuente, J. M.; Sanchez Lopez, J. C.; Garcia, M. A.; Lopez Cartes, C.; Hernando, A.; Penades, S.; Fernandez, A. *Phys. Rev. Lett.* **2004**, *93*, 087204–1–4. (b) Garcia, M. A.; Merino, J. M.; Pinel, E. F.; Quesada, A.; Venta, J.; RuizGonzalez, M. L.; Castro, G. R.; Crespo, P.; Llopis, J.; Gonzalez-Calbet, J. M.; Hernando, A. *Nano Lett.* **2007**, *7*, 1489–1494. (c) Teng, X.; Feyngenson, M.; Wang, Q.; He, J.; Du, W.; Frenkel, A. I.; Han, W.; Aronson, M. *Nano Lett.* **2009**, *9*, 3177–3184. (d) Teng, X.; Han, W. Q.; Ku, W.; Hucker, M. *Angew. Chem., Int. Ed.* **2008**, *47*, 2055–2058.